Seismological and structural constraints on the 2011-2013, M_{max} 4.6 seismic sequence at the southeastern edge of the Calabrian arc (Northeastern Sicily, Italy)

Laura Cammarata[1], Stefano Catalano[2], Salvatore Gambino[1],

Mimmo Palano[1], Francesco Pavano[2], Gino Romagnoli[2], Antonio Scaltrito[1], Giuseppe Tortorici[2]

1 Istituto Nazionale di Geofisica e Vulcanologia, Sezione di Catania, P.zza Roma 2, 95123 Catania, Italy

2 Dipartimento di Scienze Biologiche, Geologiche e Ambientali, Università di Catania, Corso Italia 57, 95129 Catania.

Submitted to: Tectonophysics

Correspondence to:

Salvatore Gambino

Istituto Nazionale di Geofisica e Vulcanologia

Sezione di Catania

P.zza Roma 2, 95123 Catania, Italy

tel. number 39-95-7165800; fax number: 39-95-435801

e-mail: Salvatore.gambino@ingv.it

Abstract

Between June 2011 and September 2013, the Nebrodi Mountains region (northeastern Sicily) was affected by a seismic swarm consisting of more than 2700 events with local magnitude $1.3 \leq M_L \leq 4.6$ and located in the 5-9 km depth interval. The seismic swarm defines a seismogenetic volume that is elongated along the E-W direction and encompasses the NW-SE-oriented tectonic boundary between the Calabrian arc (northeastward) and the Sicilide units (southwestward). Waveform similarities analysis allowed observing that ~45% of the whole dataset can be grouped into six different families of seismic events. Earthquakes grouped in families are located only in the eastern part of the seismogenetic volume, while the western sector is characterized by earthquakes with no similar waveforms. We suggest that such a feature is responsive to a change in lithology (and also on frictional parameters) as highlighted by geology (at the surface) and P-wave seismic tomography (at a depth of 10 km). Stress tensor inversions performed on FPSs indicate that the investigated region is currently subject to a nearly biaxial stress state in an extensional regime, such that crustal extension occurs along the NW-SE and along the NE-SW directions. Accordingly, mesoscale fault geometries and kinematics analyses evidence that a younger normal faulting stress regime, which controls a diffuse, quasi-radial, extensional process, led a tectonic negative inversion by replacing the pre-existing strike-slip faults array. Based on our results and findings reported in recent literature, we believe that such a crustal stretching is due to a mantle upwelling process (as evidenced by the presence of diffuse mantle-derived gas emissions) coupled with a tectonic uplift involving north-eastern Sicily since Middle Pleistocene. Moreover, seismic swarms striking the region would be related to the migration of mantle and sub-crustal fluids toward the surface along the complex network of tectonic structures cutting the crust and acting as pathways.

Keywords: *seismic swarm, multiplets, structural analysis; stress field, mantle fluids, Calabrian Arc*

Highlights

We focused on a seismic swarm striking the southeastern edge of the Calabrian arc

Waveform similarities analysis allowed us to detect six multiplet families

Multiplets occurs only in the eastern part of the seismogenetic volume

On-field we observed a reactivation of previous faults under a normal faulting regime

Seismicity is related to migration sub-crustal fluids migration

1 Introduction

North-eastern Sicily (Figure 1), located at the southern termination of the Calabrian arc, is characterized by the occurrence of temporally protracted seismic swarms. These swarms comprise small-to-moderate earthquakes and often involve shallow crustal volumes, exhibiting normal faulting features and appear related to pore pressure transients by mantle fluid flows (e.g. Scarfì et al., 2005, Giammanco et al., 2008; Camarda et al., 2016). Here, we focus on a seismic swarm that began in June 2011 and lasted until September 2013, cumulating more than 2500 events with local magnitude $1.3 \leq M_L \leq 4.6$.

The seismic events data have been collected by the INGV permanent seismic network that, since 29 June 2011, has been integrated with a mobile network consisting of 3 stations (see Cammarata et al., 2014 for additional details). In the same area, recent studies have outlined an updated morphotectonic setting of the region, highlighting a dominant NE-SW oriented extensional dynamic, inferred by several NW-SE oriented, SW-dipping rejuvenated normal faults (Pavano et al., 2015). In order to recognise possible spatial clusters and to better set the 2011 seismic swarm in such an updated tectonic frame of north-eastern Sicily, we computed 45 fault plane solutions and analysed the spatial pattern of seismicity, achieved by applying the double-difference relocation technique for 130 events by using the HypoDD algorithm (Waldhauser and Ellsworth, 2000). This latter produces more accurate locations than the standard absolute procedures, especially for spatially well-clustered seismic events (e.g. Lippitsch et al., 2005; Gambino et al., 2012).

Furthermore, in the area affected by the 2011 seismic swarm, a mesoscale structural field analysis has been carried out. This investigation enables recognising different Riedel shear fault patterns, aiming at how the rock pre-fracturing has influenced the distribution of mesoscale fault planes kinematics. As a whole, the relocated seismicity, together with both the resulting focal mechanisms and the mesoscale structural analysis data, have been compared with the active tectonic setting of the region, seeking both to test their mutual compatibility and establish the consistency with the available morphostructural data and the present stress field. As a whole, these results lead to a crustal deformation model in the frame of an updated dynamic setting of the region.

2 Tectonic and seismotectonic setting

Since the Cretaceous, the geodynamic processes of the Mediterranean region have been dominated by the still active Nubia-Eurasia plates convergence (see inset in Figure 1), which has controlled the distribution of the synorogenic tectonic domains (Malinverno and Ryan, 1986; Anderson and Jackson, 1987; Dewey et al., 1989; Doglioni, 1993; Jolivet et al., 1998). In such a geodynamic frame, northeastern Sicily represents the southern edge of the Calabrian arc (Scandone, 1979; Amodio-Morelli et al., 1976), the orocline (upper plate) related to the Ionian subduction region and connecting the southern NW-SE trending Apennines and the E-W oriented Maghrebian collisional belts (Figure 1). The geological backbone of north-eastern Sicily consists of imbricated Hercynian crystalline units, represented by low-grade to high-grade metamorphic rocks, with their Mesozoic sedimentary covers (Lentini et al., 2000; Catalano et al., 2017). These tectono-metamorphic nappes, as a whole, overlie the accretionary wedge terrains of the Sicilide Units, along an Oligo-Miocene regional thrust, which is now exposed in the Nebrodi Mountains, along a NW-SE oriented alignment, known as the Taormina Line (Figure 1; Amodio-Morelli et al., 1976; Ghisetti et al., 1991; Ghisetti and Vezzani, 1982; Lentini et al., 2000).

From the Late Miocene, due to the roll-back of the Ionian subducting slab, the Calabrian arc (Malinverno and Ryan, 1986; Patacca et al., 1990) experienced a rapid SE-ward migration, at rates

104 up to 5-8 cm/yr, until the Early Pleistocene, and of ~1 cm/yr, during the Middle-Late Pleistocene
105 (Westaway, 1993; Wortel and Spakman, 2000; Faccenna et al., 2001; Goes et al., 2004). The
106 Calabrian arc migration was accommodated by the development of high-angle left-stepping right-
107 lateral shear zones that superimposed on the previous thrust features, along its south-western end
108 (see Chiarabba and Palano, 2017 and references therein for an overview). Along this transcurrent
109 tectonic boundary the sharp lateral juxtaposition of the Maghrebian accretionary wedge, to the
110 southwest, and the European crust, to the northeast, occurs.

111 Since the Middle Pleistocene (~600 ky), the entire north-eastern Sicily region has undergone
112 an almost uniform and huge tectonic uplift (~1.1 mm/yr; Catalano and Cinque, 1995; Catalano and
113 Di Stefano, 1997), coeval with the fragmentation of the southern termination of the Calabrian arc
114 (Catalano et al., 2011; Pavano et al., 2012, 2015, 2016). Relative vertical motions between north-
115 eastern Sicily and the adjacent Sicily collision belt reactivated the southern boundary of the
116 Calabrian arc, where the negative tectonic inversion of discrete segments of the Plio-Pleistocene
117 NW-SE oriented dextral shear zones occurred (Pavano et al., 2015). The rejuvenated fault planes
118 are distributed in the surroundings of Galati Mamertino (Figure 1), where they frequently show
119 sharp basal, up to 5m-high, fresh bedrock scarps (Pavano et al., 2015), governing the geomorphic
120 features of the landscape (e.g. relief and drainage system) of the area (Pavano, 2013). The inversion
121 of the kinematic data measured on these main fault segments points to a NE-SW extension, which is
122 coherent with geodetic (Palano et al., 2015) and seismological observations (ISIDe working Group,
123 2010; Scarfì et al., 2013). This recent deformation has prominent morphological signatures
124 consisting of the vertical displacement of Late Quaternary marine terraces (Catalano and Cinque,
125 1995; Catalano and Di Stefano, 1997; Pavano et al., 2015) and of the development of triangular
126 facets and impressive dissection of raised landscapes (Pavano et al., 2015).

127 The main historical seismicity of north-eastern Sicily includes several historical moderate to
128 high magnitude earthquakes (1172, 1613, 1739, 1780, 1786, 1908 a.C.; Postpischl, 1985; Mariotti,
129 1995; Boschi et al., 1997; Guidoboni et al., 2007; Rovida et al., 2011), the latest of which struck the

Messina Strait area in the 1908 (Messina earthquake, M=7.2; Cello et al., 1982). In particular, the region of the 2011 seismic swarm was affected by two important historical earthquakes that occurred in the XVII (1613 a.C.) and XVIII centuries (1739 a.C.). Moment magnitudes of about 5.6 and 5.1 have been estimated for the two earthquakes, respectively (Rovida et al., 2011). However, the attribution of these events to any well-defined seismogenic fault is still debated.

3 Seismic data

3.1 Seismic network

Since the early 2000's, continuous monitoring of the seismic activity of eastern Sicily and southern Calabria has been performed initially by the local network installed in the framework of the "Poseidon Project", later merged into the Istituto Nazionale di Geofisica e Vulcanologia in 2001. The network consisted of a few analogic stations, equipped with three component short-period seismometers. Since 2003, the network was considerably enhanced, on one hand, with new seismic stations (Figure 1), and on the other, by replacing the old analogic station with digital 24-bit ones, equipped with broadband (40s) three-component sensors, with a dynamic range of 144 dB.

In order to improve location accuracy of the seismic swarm, a mobile seismic network of 3 stations was installed close to Naso and Longi villages (Figure 1) after the 23 June 2011 main-shock (Cammarata et al. 2014). This network worked from 29 June up to the end of September 2011.

3.2 The seismic swarm

The investigated seismic swarm (Figure 2) began in June 2011 and protracted with minor energy in 2012 and 2013. The seismic activity of 2011 lasted more than 4 months between June and October, during which we recorded more than 2500 events with local magnitude $M_L \geq 1.3$. The main event took place on 23 June 2011 at 22:02 GMT, with a magnitude of 4.6, with epicenter to the east of Galati Mamertino village at a depth of 7-8 km (red star in Figure 2). The area most notably affected is located in a radius of 10 km from the epicenter, such as including towns and

156 municipalities such as: Tortorici, Galati Mamertino, Alcara li Fusi, Militello Rosmarino (Azzaro et
157 al., 2014). The earthquake, felt by population, caused home fixtures to fall and, in some cases, even
158 the furniture moved. In the historical centers of Tortorici, Galati Mamertino and Longi, minor
159 damage also occurred in the masonry buildings (Azzaro et al., 2014). The main aftershocks were
160 recorded (all times are in GMT) on 27 June at 22:13 (M_L=3.6), 6 July at 9:08 (M_L=4.0) and 27 July
161 at 04:03 (M_L=3.5). The depth of these events generally ranges between 5 and 10 km. Between 2012
162 and 2013, we recorded ~100 earthquakes in the same area; the strongest occurred on 1 April 2012 at
163 00:57 with M_L=2.8, located ~2.3 km NW from Longi.
164
165 *3.3 Data analysis*
166 We computed accurate hypocenter locations (Figure 3) by using the double-difference
167 earthquake algorithm of Waldhauser and Ellsworth (2000) and the HypoDD routine (Waldhauser,
168 2001) on 130 events firstly located by using Hypoellipse (Lahr, 1989) and a velocity model derived
169 from Hirn et al. (1991). The algorithm takes advantage of the fact that, if the hypocentral separation
170 between two earthquakes is small enough with respect to both the event-station distance and the
171 scale length of velocity heterogeneity, the ray paths are similar along almost the entire length (Got
172 et al., 1994). Under this assumption, the differences in the travel times for two earthquakes recorded
173 at the same station can be attributed to differences in their hypocenter spatial separation. In this
174 way, errors due to inaccurately modeled velocity structure are minimized without needing station
175 corrections.
176 HypoDD initially performed a reduction of the data because it groups the events into
177 clusters of well-connected earthquakes and removes those considered outliers. In our analyses, all
178 events are connected through a network of links consisting of 11424 P- and 2362 S-wave phase
179 pairs. The average number of links per event pair was 16, while the average offset between strongly
180 linked events was of about 1.74 km. New locations reduced standard errors showing mean
181 hypocenter formal errors of 300 meters on the horizontal component and about 330 meters in the

182 vertical direction. In the relocated catalogue, the mean RMS (Root Mean square) decreased from
183 the initial value of 0.23 sec to 0.11 sec. With respect to the standard locations, the relocated events
184 show a more clustered disposition of hypocenters within a narrow range of depth, between 6 and 8.5
185 km, and distributed along a predominant E-W orientation (Figure 3).

186 In order to define prospective time changes in repeating earthquakes, waveform similarities
187 were quantitatively evaluated by adopting a cross-correlation coefficient (hereinafter referred to as
188 CCC). Following Cannata et al. (2013), the CCC values were calculated to the whole dataset of the
189 seismic swarm. In detail, the CCC analysis was computed by taking into account the waveforms
190 recorded by the vertical component of MUCR station, namely the station that recorded continuously
191 throughout the period of interest and with greater energy. The signals were treated with a band-pass
192 filter between 1 and 10 Hz. The correlations were made on time windows of 3 seconds (in order to
193 include the whole phase P and the initial part of S), and starting from the time corresponding to the
194 STA/LTA ratio. The CCC value has been calculated for each events pair. In particular, the
195 correlation has been made by comparing the time windows of 1 sec, and we shifted one with respect
196 to the other one in order to obtain the best alignment, and then the highest value of cross correlation.
197 Once obtained, the correlation matrix was applied to the method of Green and Neuberg (2006) to
198 extract the families of events characterized by similar waveforms. The correlation threshold was
199 fixed at 0.7. Such analyses have shown that ~45% of the whole dataset is grouped in six families of
200 seismic events (Figure 4). The main feature is that events belonging to families are located in the
201 eastern part of the seismogenetic volume while the western sector is characterized by earthquakes
202 without similar waveforms.

203 Furthermore, we determined the earthquake focal plane solutions (FPSs). They were
204 obtained with the FPFIT code (Reasenberg and Oppenheimer, 1985) by using the polarities of the
205 first seismic phase first motions. In detail, the FPFIT code searches the double-couple FPS that best
206 fits the set of P-wave first motion polarities for an earthquake. In some cases, FPFIT was unable to
207 converge on a unique fault-plane solution, and instead returned two or more possible solutions. If

multiple solutions for an earthquake were dissimilar (e.g. a normal solution and a strike-slip solution), they were rejected. When a unique solution, or similar multiple solutions, were obtained, the solutions were evaluated using the following criteria: i) number of polarities ≥13, ii) number of polarity discrepancies <3, iii) average uncertainty in strike, dip, and rake <20° and iv) pressure (p-) and tension (t-) axis regions that each covered <25% of the focal sphere. Fault-plane solutions that did not meet all of these criteria were rejected. Computed FPSs are reported in Table 1 and Figure 5a. FPSs show prevalently normal faulting features (95.5%), while remaining solutions are characterized by strike-slip or oblique normal faulting features (Figure 5a). Moreover, the distribution of P and T axes reveals that the former are prevailing subvertical, while the latter show a large dispersion with a prevailing concentration along the NNW-SSE orientation.

FPSs were inverted to determine the principal stress axes $\sigma_1 \geq \sigma_2 \geq \sigma_3$ and the dimensionless stress ratio R (σ_1-σ_2/σ_1-σ_3) by using an iterative approach (Vavryčuk, 2014), where in each iteration the stress field orientation is calculated and the fault plane with higher instability coefficient (out of the two possible in a focal mechanism) is selected for the next inversion iteration. Such an instability coefficient quantifies how close a fault is to an optimal orientation given a stress state and a friction coefficient (Vavryčuk, 2014). In order to avoid the sensitivity of the inversion to friction, needed in the instability constraint, the inversion was run repeatedly with friction ranging from 0.05 to 1 in steps of 0.05. For each friction, an overall instability of faults identified by the inversion was evaluated, and the friction, which produced the highest overall fault instability, was considered as optimum. In order to evaluate possible changes in the stress field, we performed different inversions by grouping the events in two main sub-datasets (namely Group A and Group B). We defined the two datasets by taking into account their CCC values since we observed that events characterized by similar waveforms are all located in the eastern part of the seismogenetic area, while no events with similar waveforms have been detected in the western part. Moreover, we performed an inversion by taking into account the whole dataset; obtained results are reported in Figure 5b and Table 2. All the resulting stress tensors are characterized by a nearly vertical σ_1 and

234 sub-horizontal σ_2 and σ_3, this last showing a NW-SE attitude. The shape ratio *R* and optimum
235 friction shows values of ~0.8 and ~0.4, respectively. These results clearly indicate that there are no
236 differences between groups A and B, hence in the following we refer to results achieved by
237 inverting the whole dataset.
238
239 **4 Structural analysis**
240 We performed a detailed field surveys data acquisition about mesoscale fault geometries and
241 kinematics in the area affected by the 2011 seismic swarm (localized between Galati Mamertino
242 and Longi villages; Figure 2) in order to detect Holocene expressions of faulting activity. To this
243 end, we collected more than 300 structural measurements, distributed on 13 measure stations
244 (Figure 2) located within a narrow belt including the main rejuvenated NW-SE oriented normal
245 fault segments affecting the seismogenetic volume (see also SGL - San Marco d'Alunzio-Galati
246 Line in Pavano et al., 2015). We utilized structural data to obtain an inversion of the stress tensors
247 from the fault kinematics. We pursued this goal by measurements that were exclusively performed
248 on tectonic features on the Liassic limestone, avoiding collecting data on the Hercynian
249 epimetamorphic basement, in order to filter any structure related to both older dynamics and
250 metamorphism processes of the crystalline units.
251 On-field collected data, grouped by both azimuth and kinematics, show a well-confined
252 distribution, especially as regards the normal faults and the right-lateral strike slip faults (Fig. 6a).
253 Normal faults are mainly distributed between N140° and N180°, showing a maximum around
254 N150°-170° and minor distributions at N10° and N70°-80° (Fig. 6a). The right-lateral strike-slip
255 faults show a similar azimuthal distribution, strongly clustering around N150°-160° and less so
256 around N120° and N170°-180° (Fig. 6a). Conversely, both reverse and left-lateral strike-slip fault
257 have a sparse azimuthal distribution. Reverse faults cluster between N40° and N70°, with minor
258 groups at N10°, N160° and N180° (Fig. 6a). The left-lateral strike-slip faults are extremely spread
259 out between N10° and N110°, without a relevant clustering, and no significant data falling between

N120° and N180° (Fig. 6a). Considering only the fault planes showing more than one generation of kinematic indicators (Fig. 6b and Table 3), a clear polyphase tectonic picture arises. In these cases, the stress tensors were obtained by inversion of the last two overlapped slickensides, neglecting, where recognized, the older ones, generally sparse and not significant. We processed separately data obtained by mesoscale measurements carried out in the footwall and in the hangingwall of the principal fault segments.

The selected fault planes show an overlapped azimuthal distribution of younger normal faults (Pitch = 90°) on previous dextral faults (Pitch = 15° and 160°) mainly around both N150°-170° and N100°-120° (Fig. 6b), whereas few faults display left-lateral strike-slip motions (Pitch = 25° and 160°) replaced by pure extensional movements at N10°-20° and N150°-160° (Fig. 6b). These distributions are consistent with the results obtained considering the entire data record (Fig. 6a), assuming that the one-kinematic shear planes are indicative of either more recent or older movements. In conclusion, we recognise two distinct, coherent structural and kinematic arrays. The oldest of the two is composed of main NW-SE oriented right-lateral faults (Pitch = 150°-180°), together with NNW-SSE and ESE-WNW oriented right-lateral strike-slip faults, minor NE-SW oriented left-lateral strike slip faults (Pitch = 15° and 165°) and NE-SW to ENE-WSW trending reverse faults (Pitch = 85°-90°). This arrangement reproduces the Riedel shear fault pattern linked to the deformation along the main NW-SE oriented right-lateral strike-slip faults and their subsidiary faults, such as the synthetic P and R shears and the antithetic P' and R'.

The main right-lateral strike-slip faults, including P and R shears, as well as the subordinate P' and R' shears (left-lateral faults), have been rejuvenated as normal faults (Pitch = 80°-100°) (Fig. 6b). These inferences are also supported by the good overlapping of the azimuthal distribution of these two groups of faults.

The fault-slip analysis results in two similar couples of moment tensor solution (Fig. 7). Like those obtained for the footwall (Fig. 7a-b), the hangingwall (Fig. 7c-d) shear planes concur with an earlier dextral kinematic with σ_1 oriented about NNE-SSW with a WNW-ESE oriented σ_3

286 (Fig. 7a and c), whereas the youngest kinematic responds to a main NE-SW extension, with an
287 almost vertical σ_1 (Fig. 7b and d). Overall, we did not recognise pronounced differences between
288 the two structural domains, suggesting a uniform response to the most recent extensional dynamics,
289 characterised by homogeneous kinematic and structural paths.
290
291 **5 Discussion**
292 We analyzed a seismic swarm (more than 2700 events with local magnitude $M_L \geq 1.3$) striking the
293 Nebrodi Mountains (north-eastern Sicily) during June 2001 - September 2013. The highest
294 magnitude reached M_L=4.6, and focal depths ranged from 5 to 9 km, with an average depth of 7-8.5
295 km. In the regional seismotectonic framework, the seismogenetic volume is located at the southern
296 edge of the Calabrian arc (Chiarabba and Palano, 2017). The earthquake swarm sequence defines an
297 E-W oriented seismogenetic area, which does not correspond to the azimuthal distribution (mainly
298 clustering around N150°-180°E) of fault segments and tectonic features mapped on field (Figure 2)
299 (Pavano et al., 2015). Results coming from CCC analysis highlighted the existence of six families
300 of multiplet seismic events that are located in the eastern part of the seismogenetic volume, while
301 the western sector is characterized by earthquakes without similar waveforms (Figure 4). Roughly
302 speaking, events within each multiplet family have nearly identical seismograms, are of similar
303 magnitude, and rupture the same fault patch more than one time. Thus, they show the characteristics
304 of repeating earthquakes and imply frictional or geometric controls on their location and size (e.g.
305 Ellsworth and Beroza, 1995) All these observations suggest a different frictional behavior between
306 the western and eastern sector of the seismogenetic volume. Indeed, at the surface, the
307 seismogenetic volume encompasses the tectonic boundary between the Hercynian crystalline units
308 of the Calabrian arc, extensively outcropping in the northeastern sector of the investigated area
309 (Figure 2) and the accretionary wedge terrains of the Sicilide units, outcropping in the southwestern
310 sector of the study area. At a depth of 10 km, at which the 2011-2013 seismic swarm events are
311 confined, such a boundary is highlighted by the seismic velocity tomography as a sharp transitional

zone between a northeastern high-velocity domain and a southwestern low-velocity one (Palano et al., 2015). In such a context, the basement high-grade metamorphic rocks seem to be characterized by frictional parameters favoring the occurrence of multiplet seismic events, while the accretionary wedge terrains do not allow the repeating rupture of the same fault patch, implying that the distinguished families of multiplet seismic events are responsive to a change in lithology (and frictional parameters) at depth. The mechanisms causing multiplet events are not completely understood; however, a number of studies have highlighted that the occurrence of persistent seismic activity can also be related to changes in pore fluid pressure that may reduce crustal strength and promote fault slip (see Miller et al., 2004 for an overview). The hypothesis is that an increase in fluid pressure reduces the effective normal stress, effectively weakening the fault and shear strength to a level below the prevailing shear stress. Camarda et al. (2016), by analyzing soil CO_2 flux measurements collected by a local network over northeastern Sicily, observed a clear spatial and temporal correlation between seismicity and gas discharge. This fact highlights the widespread occurrence of over-pressured fluid emissions at the surface over the investigated area as focused and/or diffuse gas emissions often associated with thermal fluids, therefore evidencing the migration of mantle fluids towards the surface along lithospheric pathways (e.g. faults). In light of this, we suggest that the seismic swarms striking the investigated area can be triggered by pore pressure transients due to mantle fluid flows.

Computed FPSs show prevalently normal faulting features (95.5%) with T axes showing a large dispersion with a prevailing concentration along the NNW-SSE orientation. FPSs were inverted to determine the principal stress axes $\sigma_1 \geq \sigma_2 \geq \sigma_3$ and the dimensionless stress ratio R (σ_1-σ_2/σ_1-σ_3). The resulting stress tensor is characterized by a nearly vertical σ_1 and sub-horizontal σ_2 and σ_3, this last showing a NW-SE attitude (Figure 5). This result, coupled with a stress ratio R value of ~0.8, clearly indicates a nearly biaxial stress state in an extensional regime with $\sigma_1 > \sigma_2 \cong \sigma_3$, such that crustal extension occurs along the NW-SE and along the NE-SW directions. Such a feature matches

well with recent geodetic observations (Palano et al., 2015) and with geological data acquired, in this study, by detailed field surveys.

Regarding the geological data, as above mentioned, we recognized two distinct structural and kinematic arrays. The oldest is composed of main NW-SE oriented right-lateral faults, coupled with secondary faults organized into a NNW-SSE, ESE-WNW and NE-SW to ENE-WSW arrangement. This arrangement can be related with to the progressive ESE-ward migration of the Calabrian arc that, during the Plio-Pleistocene, was accommodated by the development of a wider W-E trending lithospheric right-lateral shear zone, characterized by both NW-SE/W-E dextral faults oriented and left-lateral N-S/NE-SW fault arrays (Finetti et al., 1996; Giunta et al., 2009). The development of these fault arrays corresponds to a spatial and temporal progression from active subduction to slab detachment and recently, to the onset of compression confined along the northern Sicilian off-shore (see Chiarabba and Palano, 2017 and reference therein). Such a pre-fractured crustal domain has been involved, according to different kinematics, in a coherent and more recent dynamic. This latter, which replaces the previous one, cause a reorientation of stress axes, from horizontal, NNW-SSE trending, to vertical, leading to diffuse extensional processes and the inversion of the strike-slip faults as normal faults, implying a negative reactivation of the previous Riedel shear fault configuration. This more recent kinematic is the expression of the crustal response to the tectonic uplift that involved the north-eastern Sicily crustal domain from the Middle Pleistocene (600 ka) (Catalano and Di Stefano, 1997; Pavano et al., 2015), resulting in the fragmentation of the southern termination of the Calabrian Arc (Catalano et al., 2008; Pavano et al., 2016). Nevertheless, although the inversion of the collected mesoscale fault planes points to a prevailing NE-SW oriented extension (Figure 7), actually, a radial dispersion of the resulting kinematic vectors arises, in accordance with the FPSs inversion data. These results support the idea of mantle upwelling processes, which would occur beneath the studied region, where, at depth, sub-crustal over-pressured fluids migrate toward the surface by exploiting the crustal dense network of faults and fractures.

363 Moreover, the investigated area, localized at the westward tapering of the regional uplift pattern of
364 the Calabrian arc (Ferranti et al., 2010; Faccenna et al., 2011), can be framed in a wider (~20-30
365 km) NW-SE-oriented extensional belt. This latter would include the Madonie-Mt. Etna volcano
366 alignment, characterized by crustal stretching, as testified by previous seismological (Neri et al.,
367 2005), geodetic (Chiarabba and Palano, 2017) and geological (Billi et al., 2010) observations.
368 Several authors have explained the occurrence of these crustal stretching processes, mainly framed
369 within a prevalent compressive domain, by resorting to different mechanisms, even if this topic is
370 still an open question in recent scientific debate. Lavecchia et al. (2007) view this crustal stretching
371 as ensuing from upper crustal stretching above an active thrust belt, while Billi et al. (2010) and
372 Pavano et al., (2012) point to the reactivation of pre-existing faults and mantle upwelling.
373 Therefore, we suggest a possible relation of this extensional process with both the uplift of the
374 region, as geologically inferred (Catalano and Di Stefano, 1997; Pavano et al., 2015), and the
375 mantle upwelling (Figure 8), testified by the presence of diffuse gas emissions (Camarda et al.,
376 2016).
377
378 **6 Conclusive remarks**
379 Seismic and geological data presented in this study help improve the picture of the seismogenetic
380 pattern at the southern edge of the Calabrian arc.
381 We analyzed a seismic swarm sequence occurring in the Nebrodi Mts. area during 2011 – 2013, in
382 the 5-9 km depth interval. Such a seismic swarm defined an E-W oriented seismogenetic volume
383 encompassing the NW-SE tectonic boundary between the Hercynian crystalline units of the
384 Calabrian arc (northeastward) and the accretionary wedge terrains of the Sicilide units
385 (southwestward).
386 By analyzing the entire seismic dataset, we observed that earthquakes showing similar waveforms
387 are located only on the eastern part of the seismogenetic volume, evidencing the responsivity to
388 changes in lithology frictional parameters at depth. Structural analysis evidences that the structural

path of the investigated area, after an early stage dominated by dextral strike-slip faulting, underwent a reactivation of the same Riedel shear planes path under an extensional dynamic. Stress tensor inversions performed on FPSs and fault slip data indicate that the investigated area is currently subject to a nearly biaxial stress state in an extensional regime, such that crustal extension occurs along both NW-SE and NE-SW directions.

This prevailing extension can be related to a mantle upwelling process (as evidenced by the presence of diffuse mantle-derived gas emissions) coupled with a tectonic uplift involving north-eastern Sicily since the Middle Pleistocene. Thus, the seismic swarms striking the Nebrodi Mountains would be related to the mantle upwelling and the migration of sub-crustal over-pressured fluids toward the surface along the complex network of tectonic structures that cut the crust and act as pathways.

Figure Captions

Figure 1. a) Simplified tectonic map of Sicily and surrounding areas. The yellow box indicates the area reported on panel b. The Maghrebian Chain and the Calabro Peloritanian Arc are parts of the Apennine-Maghrebian orogen (see inset), a large-scale fold-and-thrust belt formed during the Neogene-Quaternary convergence between Nubia and Eurasia plates. b) Simplified tectonic map of North-East Sicily. Epicentres of earthquakes occurring in the study region since 1000 A.D. are reported as blue circles (see legend in the bottom right corner). Data are from the CPTI catalogue (Rovida et al., 2011); magnitude completeness of the catalogue was 6.4, 5.8, 4.9 and 4.3 since 1300, 1530, 1700 and 1895, respectively. Abbreviations are: GM, Galati Mamertino; Ta, Taormina; MS, Messina Strait; ATLF, Aeolian-Tindari-Letojanni Fault System; TL, Taormina Line. On legend: (1) Major reverse faults, (2) oblique and dip-slip faults, (3) continuous and (4) mobile seismic stations. The dashed rectangle indicates the main study area of the present work.

Figure 2. Geological map of the region affected by the 2011-2013 seismic swarm, showing the main geological units and structural features. The standard location of the hypocentres of the analysed seismic events, the position of the main shock (red star) and the distribution of the structural measure stations are also reported.

Figure 3. Map and vertical cross-sections of the seismicity relocated by using the HypoDD code.

Figure 4. Results of cross correlation: (a) the correlation matrix where the events with a correlation major of 0.7 are grouped in families; (b) example of seismic signals correlation related to family 1. (c) Map and (d) EW section of relocated events showing families position. White circles represent events out of families.

Figure 5. (a) Map of the investigated area with fault plane solutions computed in this study. FPSs are colored according to the family events (see Table 1 for numbers and additional details). Right-hand panels show the P- and T-axes distribution on equal-area lower hemisphere projection (upper panel) and a ternary plot of FPSs (lower panel). Each point is plotted based on the plunge of the *P*-, *T*- and *B*-axes of the mechanism (Frohlich 1992). The dashed line divides the triangle into faulting styles based on definitions by Zoback (1992): NF is normal faulting, NS is normal and strike-slip, SS is strike-slip, TS is thrust and strike-slip, TF is thrust faulting and *U* is undefined. (b) Stress tensor inversion results for groups A, B and All (see the main text for details) reported as confidence limits of each principal stress directions and the dimensionless stress ratio R.

Figure 6. a) Azimuthal distribution of the entire dataset of shear planes distinguished by kinematic; b) Azimuthal distribution of the selected shear planes showing two generations of striae, distinguished by kinematic.

441

442 **Figure 7**. Moment tensor solutions resulting by fault inversion analysis of shear planes: a) plot
443 results from older and (b) the youngest kinematics obtained from the data falling within the
444 footwall; c) plot results from older and (d) the youngest kinematics from data falling within the
445 hangingwall. Black dots indicate the rake values and black arrows the direction and the sense of
446 movement. Blue squares represent the main axes of stress: 1= σ_3; 2= σ_2; 3= σ_1.

447

448 **Figure 8.** Schematic transect across the boundary between Nebrodi Mts. and Peloritani Mts., at the
449 southern termination of the Calabrian, where diffuse normal faulting along previous thrust and high-
450 angle strike-slip faults occurs. The Mantle upwelling, the fluid migration towards the surface and
451 the fluid overpressure region at depth, invoked to model our results, are drawn.

452

453 **Tables**

454 **Table 1.** FPSs computed in this study. Date is in format day-month-year; O.T.=origin time (hour
455 and minute); latitude north and longitude east; depth in km; M=magnitude.

456

457 **Table 2.** Results of stress inversions. The errors are the maximum differences between the results
458 calculated for the noise-free and noisy focal mechanisms with 1000 random realizations (see
459 Vavryčuk, 2014 for additional details).

460

461 **Table 3.** Selected shear planes showing two groups of slickensides, with clear kinematics
462 overlapping. The data gained on the footwall and hangingwall block are distinguished.

463 **References**

464 Amodio-Morelli L, Bonari G, Colonna V, Dietrich D, Giunta G, Ippolito F, Liguori V, Lorenzoni S,
465 Paglionico A, Perrone V, Piccarreta G, Russo M, Scandone P, Zanettin-Lorenzoni E,
466 Zappetta A., 1976. L'Arco Calabro-peloritano nell'orogene appenninico-maghrebide. Mem.
467 Soc. Geol. It. 17; 1-60.

468 Anderson H.A., Jackson J.A., 1987. The deep seismicity of the Tyrrhenian Sea. Geophys J R Astron
469 Soc, 91; 613-637.

470 Azzaro R., D'Amico S., Mostaccio A., Scarfì L., Tuvè T., Manni M., 2014. Terremoti con effetti
471 macrosismici in Sicilia orientale nel periodo Gennaio 2009 - Dicembre 2013. Quaderni di
472 Geofisica, n. 120. ISSN 1590-2595.

473 Billi, A., Presti, D., Orecchio, B., Faccenna, C., Neri, G., 2010. Incipient extension along the active
474 convergent margin of Nubia in Sicily, Italy: Cefal-Etna seismic zone. Tectonics 29, 4; n.
475 TC4026.

476 Boschi, E., Guidoboni, E., Ferrari, G., Valensise, G., Gasperini, P., 1997. Catalogo dei forti
477 terremoti in Italia dal 461 A.C. al 1990. Istituto Nazionale di Geofisica, Roma, 644 pp.

478 Camarda, M., De Gregorio, S., Di Martino, R.M.R., Favara, R., 2016. Temporal and spatial
479 correlations between soil CO_2 flux and crustal stress. J. Geophys. Res.: Solid Earth 121, 10;
480 7071-7085.

481 Cammarata, L., Gambino, S., Maiolino, V., Messina, A., Rapisarda, S., Scaltrito, A., Zuccarello L.,
482 2014. Contributo delle reti sismiche mobili durante i periodi di crisi: L'esempio della
483 sequenza dei monti Nebrodi del 2011. Rapporti Tecnici INGV n° 287, ISSN 2039-7941

484 Cannata, A., Alparone, S., Ursino, A., 2013. Repeating volcano-tectonic earthquakes at Mt. Etna
485 volcano (Sicily, Italy) during 1999-2009. Gondwana Research 24, 1223-1236.

486 Catalano, S., Cinque, A., 1995. L'evoluzione neotettonica dei Peloritani settentrionali (Sicilia nord-
487 orientale): il contributo di una analisi geomorfologica preliminare. Studi Geologici Camerti,
488 Vol. Spec. 1995/2; 113-123.

489 Catalano, S., Cirrincione, R., Mazzoleni, P., Pavano, F., Pezzino, A., Romagnoli, G., Tortorici, G.,
490 2017. The effects of a Meso-Alpine collision event on the tectono-metamorphic evolution of
491 the Peloritani mountain belt (eastern Sicily, southern Italy). Geological Magazine.

492 Catalano, S., Di Stefano, A., 1997. Sollevamento e tettogenesi Pleistocenica lungo il margine
493 tirrenico dei Monti Peloritani: integrazione dei dati geomorfologici, strutturali e
494 biostratigrafici. Il Quaternario 10; 337-342.

495 Catalano, S., De Guidi, G., Monaco, C., Tortorici, G., Tortorici, L., 2008. Active faulting and
496 seismicity along the Siculo-Calabrian rift zone. Tectonophysics 453; 177-192.

497 Catalano, S., Pavano, F., Romagnoli, G., Tortorici, G., 2011. The role of mantle diapirism in the
498 Late Quaternary tectonics and dynamics of eastern Sicily. GNGTS 30° Convegno
499 Nazionale, Trieste 14-17 Novembre 2011. Consiglio Nazionale delle Ricerche. Riassunti
500 estesi delle comunicazioni; 117-122.
501 Cello, G., Guerra, I., Tortorici, L., Turco, E., Scarpa, R., 1982. Geometry of the neotectonics stress
502 field in southern Italy: geological and seismological evidence. J. of Struct. Geol. 4; 385-393.
503 Chiarabba, C., Palano, M., 2017. Progressive migration of slab break-off along the southern
504 Tyrrhenian plate boundary: Constraints for the present day kinematics. J. Geodyn. 105; 51-
505 61.
506 Dewey, J.F., Helman, M.L., Turco, E., Hutton, D.H.W., Knott, S.D., 1989. Kinematics of the
507 western Mediterranean. Alpine Tectonics, Geol. Soc. Spec. Publ. 45; 265-283.
508 Doglioni, C., 1993. Geological evidence for a global tectonic polarity. J. Geol. Soc. Lond. 150,991–
509 1002.
510 Ellsworth, W.L., Beroza, G.C., 1995. Seiamic evidence for an earthquake nucleation phase. Science
511 268, 5212; 851-855.
512 Faccenna, C., Becker T. W., Lucente F. P., Jolivet L., Rossetti F. 2001, History of subduction and
513 back-arc extension in the Central Mediterranean, Geophys. J. Int., 145, 3; 809-820.
514 Faccenna, C., Molin, P., Orecchio, B., Olivetti, V., Bellier, O., Funiciello, F., Minelli, L., Piromallo,
515 C., Billi, A., 2011. Topography of the Calabria subduction zone (southern Italy): Clues for
516 the origin of Mt. Etna. Tectonics, 30; TC1003. doi:10.1029/2010TC002694.
517 Ferranti, L., Antonioli, F., Anzidei, M., Monaco, C., Stocchi, P., 2010. The timescale and spatial
518 extent of vertical tectonic motions in Italy: Insights from relative sea-level changes studies.
519 J. Virt. Expl. 36. DOI: 10.3809/jvirtex.2009.00255
520 Finetti, I.R., Lentini, F., Carbone, S., Catalano, S., Del Ben, A., 1996. Il Sistema Appennino
521 Meridionale-Arco Calabro-Sicilia nel Mediterraneo centrale: studio geologico-geofisico.
522 Boll. Soc. Geol. It. 115; 529-559.
523 Frohlich, C., 1992. Triangle diagrams: ternary graphs to display similarity and diversity of
524 earthquake focal mechanisms, Phys. Earth planet. Inter., 75; 193–198, doi:10.1016/0031-
525 9201(92)90130-N.
526 Gambino, S., Milluzzo, V., Scaltrito, A., Scarfì, L., 2012. Relocation and focal mechanisms of
527 earthquakes in the south-central sector of the Aeolian Archipelago:new structural and
528 volcanological insights. Tectonophysics 524–525; 108–115.

529 Giammanco, S., Palano, M., Scaltrito, A., Scarfì, L., Sortino, F., 2008. Possible role of fluid
530 overpressure in the generation of earthquake swarms in active tectonic areas: The case of the
531 Peloritani Mts. (Sicily, Italy). J. Volcanol. Geotherm. Res. 178, 4; 795-806.
532 Giunta, G., Luzio, D., Agosta, F., Calò, M., Di Trapani, F., Giorgianni, A., Oliveri, E., Orioli, S.,
533 Perniciaro, M., Vitale, M., Chiodi, M., Adelfio, G., 2009. An integrated approach to
534 investigate the seismotectonics of northern Sicily and southern Tyrrhenian. Tectonophysics
535 476; 13–21. http://dx.doi.org/10.1016/j.tecto.2008.09.031.
536 Ghisetti F, Pezzino A, Atzori P, Vezzani L. 1991. Un approccio strutturale per la definizione della
537 Linea di Taormina: risultati preliminari. Memorie della Società Geologica Italiana 47; 273-
538 289.
539 Ghisetti, F., Vezzani, L., 1982. The recent deformation mechanisms of the Calabrian Arc. Earth Ev.
540 Sc., 3, 197-206.
541 Goes, S., Giardini, D., Jenny, S., Hollenstein, C., Kahle, H.G., Geiger, A., 2004. A recent
542 reorganization in the south-central Mediterranean. Earth Planet Science Lett. 226; 335–345.
543 Got, J.L., Fréchet, J., Klein, F.W., 1994. Deep fault plane geometry inferred from multiplet relative
544 relocation beneath the south flank of Kilauea. J. Geophys. Res., 99; 15375−15386.
545 Green, D., Neuberg, J., 2006, Waveform classification of volcanic low frequency swarms and its
546 implication, J. Volcanol. Geotherm. Res., 153; 51-63.
547 Guidoboni, E., Ferrari, G., Mariotti, D., Comastri, A., Tarabusi, G., Valensise, G., 2007.
548 CFTI4Med, Catalogue of Strong Earthquakes in Italy (461 B.C.-1997) and Mediterranean
549 Area (760 B.C.-1500). INGV-SGA. http://storing.ingv.it/cfti4med/
550 Hirn, A., Nercessian, A., Sapin, M., Ferrucci, F., Wittlinger, G., 1991. Seismic heterogeneity of Mt
551 Etna:structure and activity. Geophys. J. Int. 105, 139-153. doi:10.1111/j.1365-
552 246X.1991.tb03450.x.
553 ISIDEe Working Group (INGV), 2010. Italian seismological Instrumental and parametric database:
554 http://iside.rm.ingv.it.
555 Jolivet, L., Faccenna, C., Goffè, B., Mattei, M., Rossetti, F., Brunet, C., Storti, F., Funiciello, R.,
556 Cadet, J.P., D'Agostino, N., Parra, T., 1998. Midcrustal shear zones in postorogenic
557 extension: Example from the northern Tyrrhenian Sea. J. Geophis. Res.: Solid Earth, 103, 6;
558 12123-12160.
559 Lahr, J.C., 1989. HYPOELLIPSE/VERSION 2.0: A computer program for determining local
560 earthquake hypocentral parameters, magnitude, and first motion pattern. U.S. Geol. Survey,
561 Open-File Report 89/116; 81 pp.

562 Lavecchia, G., Ferrarini, F., de Nardis, R., Visini, F., Barbano, M.S., 2007. Active thrusting as a
563 possible seismogenic source in Sicily (Southern Italy): Some insights from integrated
564 structural-kinematic and seismological data. Tectonophysics 445; 145-167.
565 Lentini, F., Catalano, S., Carbone, S., 2000. Nota illustrativa della Carta geologica della Provincia
566 di Messina (Sicilia Nord-Orientale), scala 1:50.000. S.EL.CA (Ed.): Firenze; 70 pp.
567 Lippitsch, R., White, R., Soosalu, H., 2005. Precise hypocenter relocation of microearthquakes in a
568 high- temperature geothermal field: the Torfajökull central volcano, Iceland. Geophys. J. Int.
569 160, 371-388.
570 Malinverno, A., Ryan, W.B.F., 1986. Extension in the Tyrrhenian Sea and shortening in the
571 Apennines as result of arc migration driven by slab sinking in the lithosphere. Tectonics 5;
572 227–245.
573 Mariotti, D., 1995. An unknown destructive earthquake in 18th century Sicily. In: E. Boschi, R.
574 Funiciello, E. Guidoboni and A. Rovelli (eds.), Earthquakes in the past: multidisciplinary
575 approaches. Ann. Geofis. 38, 5-6; 551-554.
576 Miller, S.A., Collettini,C., Chiaraluce, L., Cocco, M., Barchi, M., Kaus, B.J.P., 2004. Aftershocks
577 driven by a high-pressure CO2 source at depth. Nature 427, 6976; 724–727.
578 Neri, G., Oliva, G., Orecchio, B., Presti, D., 2006. A possible seismic gap within a highly
579 seismogenic belt crossing Calabria and eastern Sicily, Italy, Bull. Seismol. Soc. Am. 96, no.
580 4A, 1321–1331, doi: 10.1785/0120050170.
581 Palano, M., Schiavone, D., Loddo, M., Neri, M., Presti, D., Quarto, R., Totaro, C., Neri, G., 2015.
582 Active upper crust deformation pattern along the southern edge of the Tyrrhenian
583 subduction zone (NE Sicily): Insights from a multidisciplinary approach. Tectonophysics
584 657; 205-2018.
585 Pavano, F., 2013. Late Quaternary deformation of NE Sicily from relief and drainage system
586 analysis. Rendiconti Online della Società Geologica Italiana 29; 134-137.
587 Pavano, F., Catalano, S., Romagnoli, G., Tortorici, G., 2012. Dynamics and seismotectonics of NE
588 Sicily. Rend. Online Soc. Geol. It. 21; 241-243.
589 Pavano, F., Romagnoli, G., Tortorici, G., Catalano, S., 2015. Active tectonics along the Nebrodi-
590 Peloritani boundary in northeastern Sicily (Southern Italy). Tectonophysics 659; 11: doi:
591 10.1016/j.tecto.2015.07.024.
592 Pavano, F., Pazzaglia, F.J., Catalano, S., 2016. Knickpoints as geomorphic markers of active
593 tectonics: A case study from northeastern Sicily (southern Italy). Lithosphere 8, 6; 633-648.
594 Doi: 10.1130/L577.1.

595 Patacca, E., Sartori, R., Scandone, P., 1990. Tyrrhenian basin and Apenninic arcs. Kinematic
596 relations since late Tortonian times. Mem. Soc. Geol. Ital. 45; 425–451.
597 Postpischl, D., 1985. Catalogo dei terremoti italiani dall'anno 1000 al 1980. CNR, P.F.
598 Geodinamica, Graficoop, Bologna; 239 pp.
599 Reasenberg, P., Oppenheimer, D., 1985. FPFIT, FPPLOT and FPPAGE: FORTRAN computer
600 programs for calculating and displaying fault plane solutions. U.S. Geol. Surv. Open File
601 Rep. 85/739; 109 pp.
602 Rovida, A., Camassi, R., Gasperini, P., Stucchi, M., (a cura di), 2011. CPTI11, la versione 2011 del
603 Catalogo Parametrico dei Terremoti Italiani. Milano, Bologna,
604 http://emidius.mi.ingv.it/CPTI
605 Scandone, P., 1979. Origin of the Tyrrhenian Sea and Calabrian Arc. Boll. Soc. Geol. It. 98; 27-34.
606 Scarfì, L., Langer, H., Scaltrito, A., 2005. Relocation of microearthquake swarms in the Peloritani
607 mountains – implications on the interpretation of seismotectonic patterns in NE Sicily, Italy.
608 Geophys. J. Int. 163; 225–237, doi: 10.1111/j.1365-246X.2005.02720.x.
609 Scarfì, L., Messina, A., Cassisi, C., 2013. Sicily and southern Calabria focal mechanism database: a
610 valuable tool for local and regional stress-field determination. Annals of Geophysics, 56; 1-
611 16.
612 Vavryčuk, V., 2014. Iterative joint inversion for stress and fault orientations from focal
613 mechanisms. Geophysical Journal International 199, 1; 69-77.
614 Waldhauser, F., Ellsworth, W.L., 2000. A double-difference earthquake location algorithm: Method
615 and application to the northern Hayward fault. Bull. Seism. Soc. Am. 90; 1353-1368.
616 Waldhauser, F., 2001. HypoDD: A computer program to compute double-difference earthquake
617 locations. U.S. Geol. Surv. Open-File Report; 1-113.
618 Westaway, R., 1993. Quaternary uplift of southern Italy. Journal of Geophysical Research 98, B12;
619 21,741-21,772.
620 Wortel, M.J.R., Spakman, W., 2000, Geophysics - Subduction and slab detachment in the
621 Mediterranean-Carpathian region, Science, 290, 5498; 1910-1917.
622 Zoback, M.L., 1992. First- and second-order patterns of stress in the lithosphere: the World Stress
623 Map Project. J. Geophys. Res., 97(B8); 11 703-11 728.

Table 1

Click here to download Table: Table_01.docx

N	Date	O.T.	Lat. (°E)	Lon. (°N)	M_L	Depth (km)	Strike (°)	Dip (°)	Rake (°)	Family
1	11/06/2011	15:15	38.0089	14.8259	2.2	8.36	75	40	-70	
2	23/06/2011	22:02	38.0331	14.7693	4.6	8.39	65	45	-130	
3	24/06/2011	00:46	38.0343	14.7824	2.7	8.29	50	60	-120	2
4	24/06/2011	04:08	38.0234	14.7653	2.6	8.03	35	40	-130	
5	24/06/2011	14:37	38.0444	14.7527	2.8	6.03	260	70	-60	
6	24/06/2011	17:57	38.0267	14.7835	2.7	8.36	50	35	-120	2
7	25/06/2011	18:35	38.0292	14.7512	2.6	7.70	50	45	-120	
8	26/06/2011	01:18	38.0243	14.7592	2.5	7.75	130	35	-80	
9	26/06/2011	02:37	38.0261	14.7657	1.8	8.46	75	75	-70	5
10	27/06/2011	05:23	38.0228	14.7421	3.3	8.07	40	65	-120	
11	27/06/2011	07:15	38.0288	14.7525	2.7	8.07	100	25	-110	
12	27/06/2011	17:42	38.0204	14.7652	2.7	8.43	20	30	-140	
13	27/06/2011	22:13	38.0250	14.7382	3.6	7.83	40	60	-120	
14	28/06/2011	00:43	38.0221	14.7481	2.6	8.10	5	55	-110	
15	28/06/2011	08:25	38.0263	14.7753	3.0	8.48	60	50	-100	1
16	28/06/2011	11:54	38.0242	14.7634	2.9	8.19	45	50	-120	
17	29/06/2011	09:04	38.0243	14.7402	3.2	8.04	135	35	-80	
18	29/06/2011	19:15	38.0276	14.7453	3.3	7.87	105	75	-140	
19	30/06/2011	09:49	38.0269	14.7403	2.7	7.45	55	45	-140	
20	30/06/2011	14:32	38.0340	14.7560	2.4	7.88	40	40	-130	
21	30/06/2011	21:02	38.0221	14.7501	2.9	7.78	40	45	-100	
22	02/07/2011	19:33	38.0235	14.7706	2.7	8.40	35	55	-80	
23	04/07/2011	09:36	38.0316	14.7727	3.3	8.14	45	60	-100	1
24	05/07/2011	14:46	38.0279	14.7715	2.5	7.71	115	45	-90	3
25	06/07/2011	09:08	38.0309	14.7798	4.0	8.47	40	55	-110	
26	06/07/2011	09:52	38.0361	14.7614	2.6	7.75	35	70	-120	
27	06/07/2011	15:56	38.0294	14.7694	2.5	8.43	35	60	-110	1
28	06/07/2011	23:58	38.0233	14.7692	2.4	7.79	165	35	-70	3
29	07/07/2011	01:01	38.0311	14.7781	3.2	8.34	40	70	-90	1
30	08/07/2011	13:11	38.0272	14.7735	2.4	7.50	155	30	-50	3
31	09/07/2011	19:05	38.0291	14.7797	2.7	8.43	50	40	-110	1
32	09/07/2011	19:05	38.0290	14.7806	2.9	8.36	40	45	-120	1
33	10/07/2011	06:14	38.0279	14.7809	2.3	8.27	70	40	-130	2
34	11/07/2011	01:16	38.0260	14.7676	2.6	7.81	-40	60	-100	6
35	11/07/2011	04:49	38.0375	14.7316	1.8	6.79	85	45	-70	
36	15/07/2011	13:43	38.0310	14.7639	1.6	7.26	60	50	-100	5
37	23/07/2011	06:14	38.0247	14.7787	2.8	7.85	55	55	-130	
38	23/07/2011	09:02	38.0526	14.7980	2.0	6.77	105	70	-70	
39	27/07/2011	04:03	38.0262	14.7668	3.5	7.72	150	30	-80	6
40	07/08/2011	21:50	38.0284	14.7777	2.4	8.16	40	55	-110	1
41	25/08/2011	13:07	38.0286	14.7837	2.4	8.18	70	25	-140	2
42	31/03/2012	13:09	38.0285	14.7439	2.4	8.21	-10	55	-130	
43	01/04/2012	00:57	38.0283	14.7441	2.8	8.29	15	60	-90	
44	04/09/2013	09:23	38.0185	14.8341	2.1	9.03	95	45	-20	4
45	06/09/2013	19:39	38.0167	14.8309	1.6	9.12	165	35	-160	4

Table 2

Click here to download Table: Table_02.docx

Dataset	N° FPS	σ_1 Az./pl.	σ_2 Az./pl.	σ_3 Az./pl.	R	Friction
A	21	257°/75° ± 17°	56°/14° ± 88°	147°/5° ± 88°	0.83 ± 50%	0.35
B	24	236°/79° ± 15°	57°/11° ± 68°	327°/0° ± 68°	0.78 ± 40%	0.40
All	45	245°/78° ± 12°	56°/12° ± 59°	147°/2° ± 59°	0.84 ± 31%	0.40

Table 3

Click here to download Table: Table_03.docx

Measure St.	Azimuth (RHR) (°)	Dip (°)	Pitch 1 (°)	Kin. 1 (°)	Pitch 2 (°)	Kin. 2 (°)
FOOTWALL						
S1	10	85 E	20	Sx	50	N
S2	110	70 N	0	Dx	120	N
S2	105	50 N	5	Dx	100	N
S2	100	50 N	0	Dx	20	Dx
S2	160	70 E	25	Dx	100	N
S3	165	80 W	170	Dx	25	Dx
S3	175	75 E	5	Dx	90	N
S3	150	80 E	130	Sx	30	Sx
S3	160	70 E	0	Dx	165	Sx
HANGINGWALL						
S4	20	80 W	30	Sx	60	N
S4	135	80 SW	170	Dx	135	N
S5	160	70 E	50	Dx	100	N
S5	160	60 E	50	Dx	100	N
S5	150	60 NE	45	Dx	100	N
S5	100	85 N	10	Dx	60	N
S6	60	70 SE	20	Sx	50	N
S6	150	60 NE	5	Dx	140	Dx
S7	155	30 E	100	N	85	N
S8	160	30 E	115	N	160	Sx
S8	160	70 E	120	N	70	N
S9	65	80 SE	80	I	100	I
S9	150	80 NE	0	Dx	50	N
S9	120	60 SW	20	Dx	150	Dx
S10	80	60 S	170	Dx	100	N
S11	160	60 E	95	N	110	N
S11	20	75 E	15	Sx	70	N
S11	120	60 NE	160	Dx	60	N
S11	0	80 E	10	Dx	70	N
S11	175	75 E	0	Dx	130	N
S11	155	80 NE	0	Dx	90	N
S11	160	75 E	5	Dx	60	N
S11	165	85 E	0	Dx	65	N
S12	170	70 W	5	Dx	100	N
S12	165	75 W	5	Dx	95	N
S12	150	85 SW	110	N	100	N
S12	155	80 W	130	N	100	N
S12	45	60 NW	70	N	100	N
S12	0	60 W	130	N	80	N

Figure 1

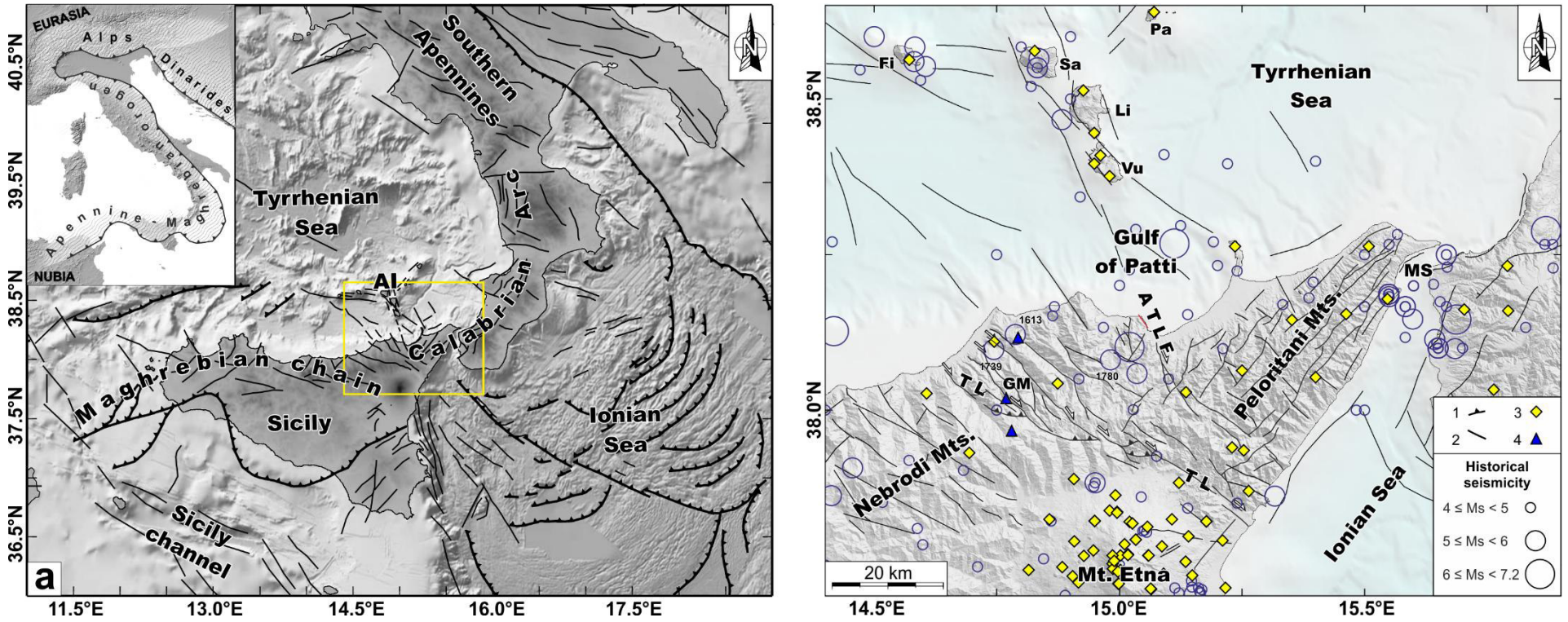

Figure 1. a) Simplified tectonic map of Sicily and surrounding areas. The yellow box indicates the area reported on panel b. The Maghrebian Chain and the Calabro Peloritanian Arc are parts of the Apennine-Maghrebian orogen (see inset), a large-scale fold-and-thrust belt formed during the Neogene-Quaternary convergence between Nubia and Eurasia plates. b) Simplified tectonic map of North-East Sicily. Epicentres of earthquakes occurring in the study region since 1000 A.D. are reported as blue circles (see legend in the bottom right corner). Data are from the CPTI catalogue (Rovida et al., 2011); magnitude completeness of the catalogue was 6.4, 5.8, 4.9 and 4.3 since 1300, 1530, 1700 and 1895, respectively. Abbreviations are: GM, Galati Mamertino; Ta, Taormina; MS, Messina Strait; ATLF, Aeolian-Tindari-Letojanni Fault System; TL, Taormina Line. On legend: (1) Major reverse faults, (2) oblique and dip-slip faults, (3) continuous and (4) mobile seismic stations. The dashed rectangle indicates the main study area of the present work.

Figure 2

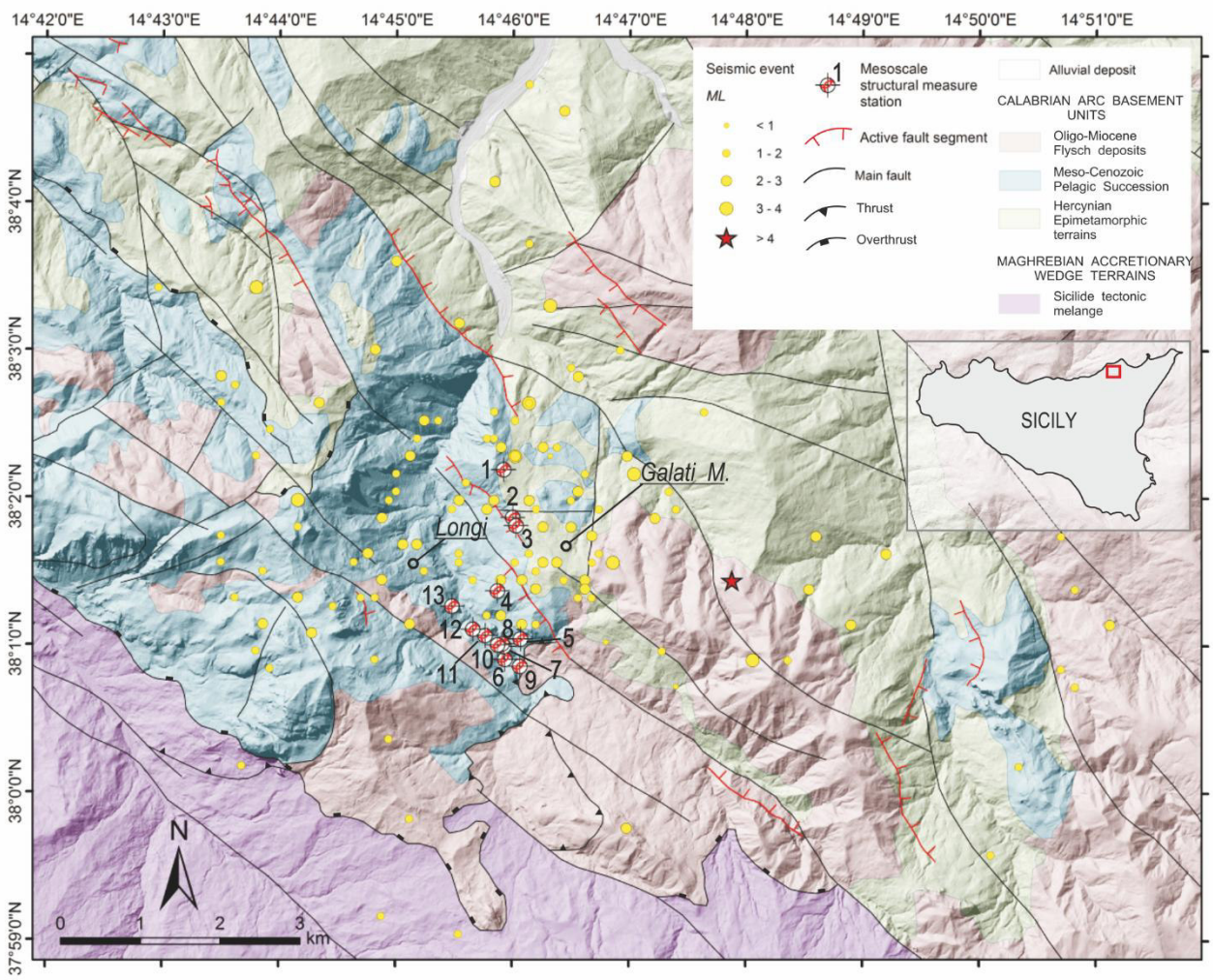

Figure 2. a) Geological map of the region affected by the 2011-2013 seismic swarm, showing the main geological units and structural features. The standard location of the hypocentres of the analysed seismic events, the position of the main shock (red star) and the distribution of the structural measure stations are also reported.

Figure 3

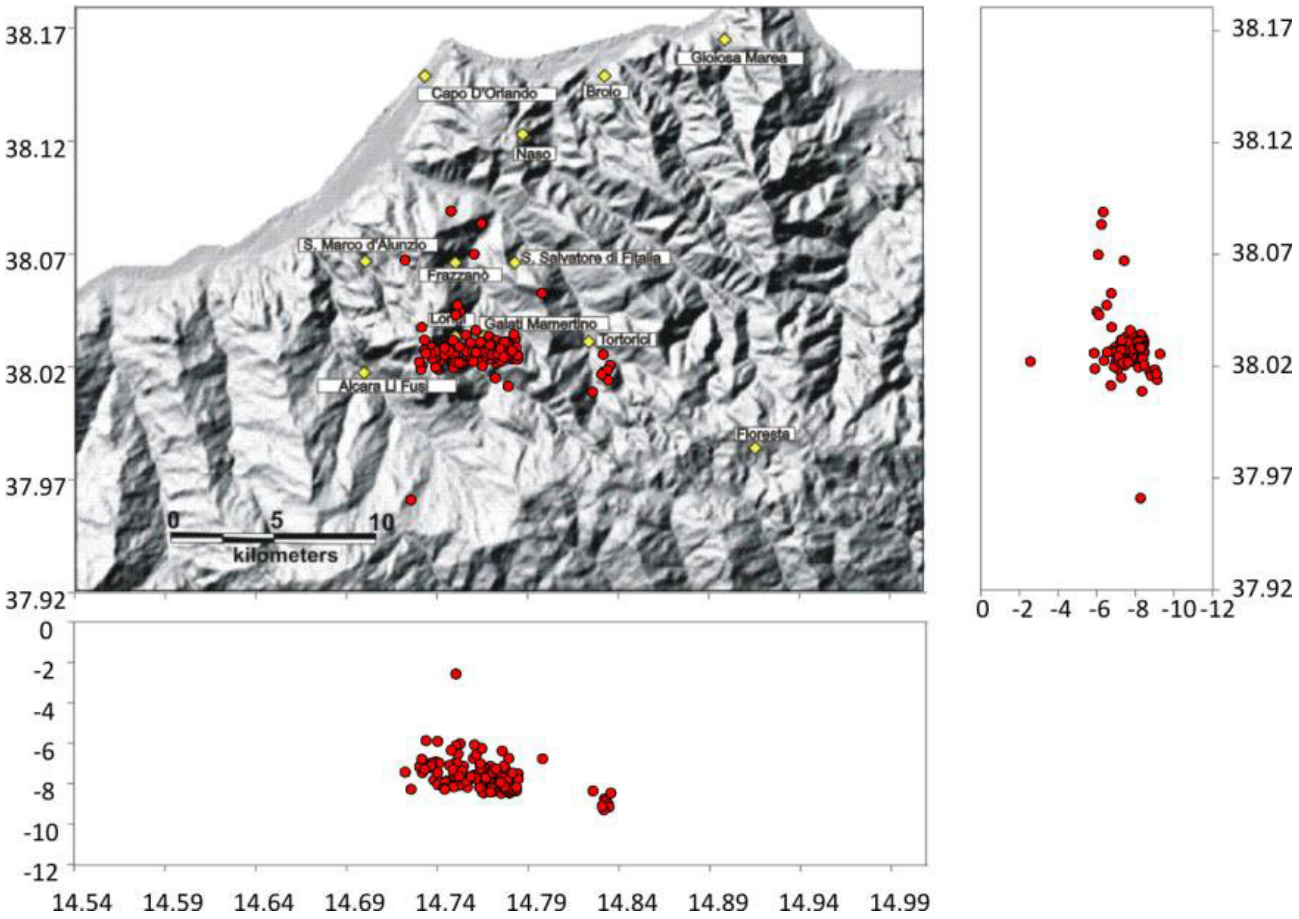

Figure 3. Map and vertical cross-sections of the seismicity relocated by using the HypoDD code.

Figure 4

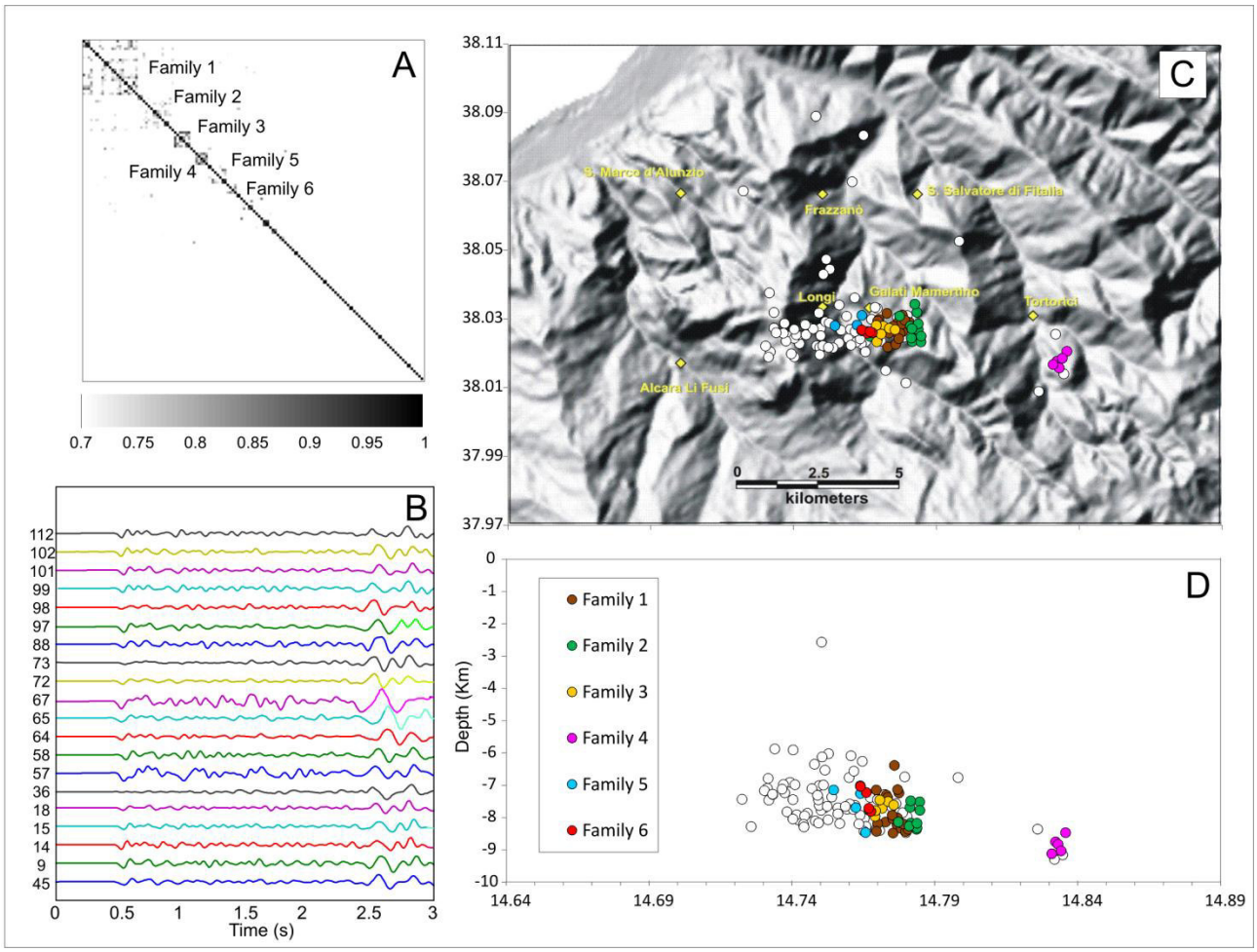

Figure 4. Results of cross correlation: (a) the correlation matrix where the events with a correlation major of 0.7 are grouped in families; (b) example of seismic signals correlation related to family 1. (c) Map and (d) EW section of relocated events showing families position. White circles represent events out of families.

Figure 5

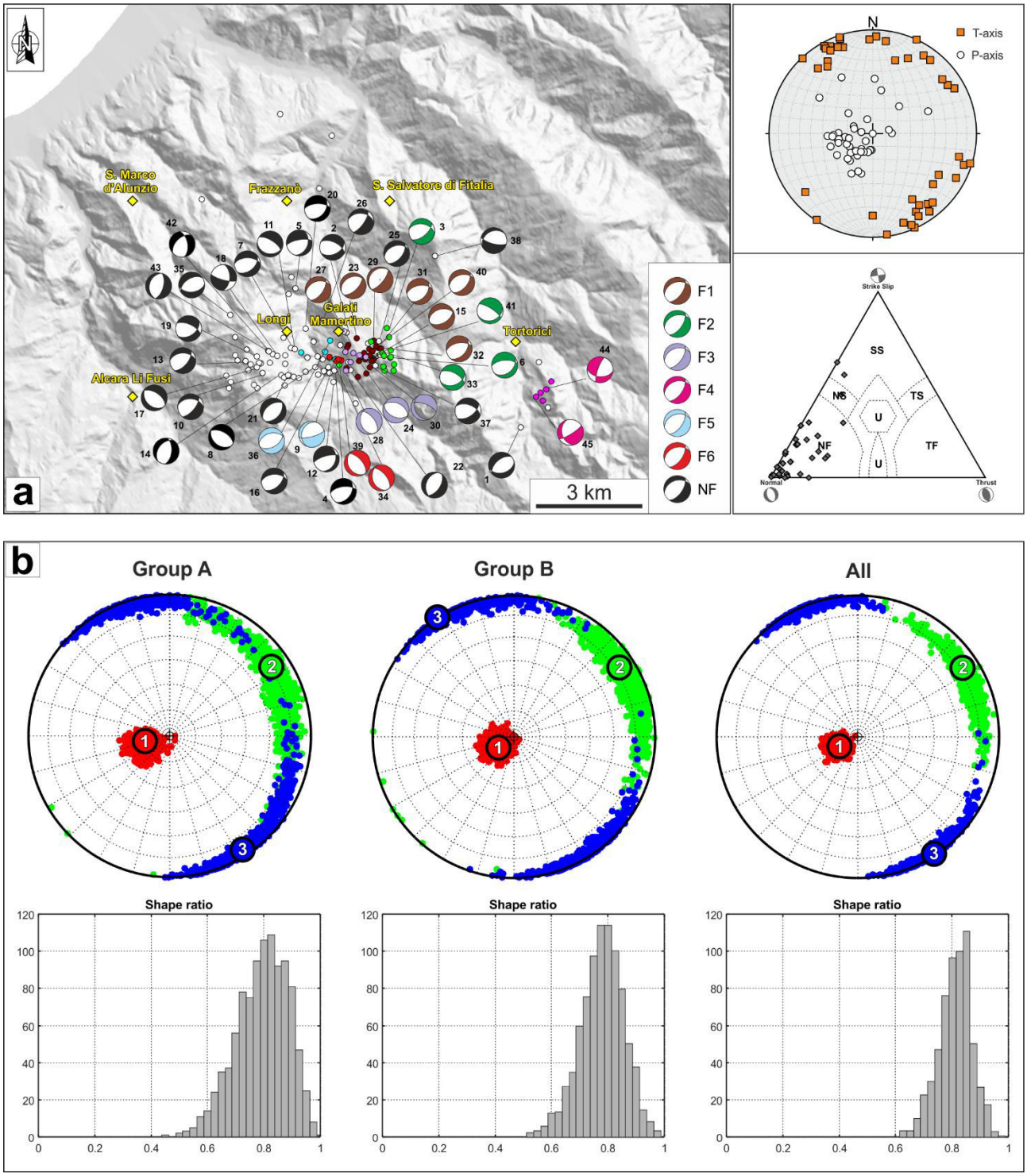

Figure 5. (a) Map of the investigated area with fault plane solutions computed in this study. FPSs are colored according to the family events (see Table 1 for numbers and additional details). Right-hand panels show the P- and T-axes distribution on equal-area lower hemisphere projection (upper panel) and a ternary plot of FPSs (lower panel). Each point is plotted based on the plunge of the *P*-, *T*- and *B*-axes of the mechanism (Frohlich 1992). The dashed line divides the triangle into faulting styles based on definitions by Zoback (1992): NF is normal faulting, NS is normal and strike-slip, SS is strike-slip, TS is thrust and strike-slip, TF is thrust faulting and *U* is undefined. (b) Stress tensor inversion results for groups A, B and All (see the main text for details) reported as confidence limits of each principal stress directions and the dimensionless stress ratio R.

Figure 6

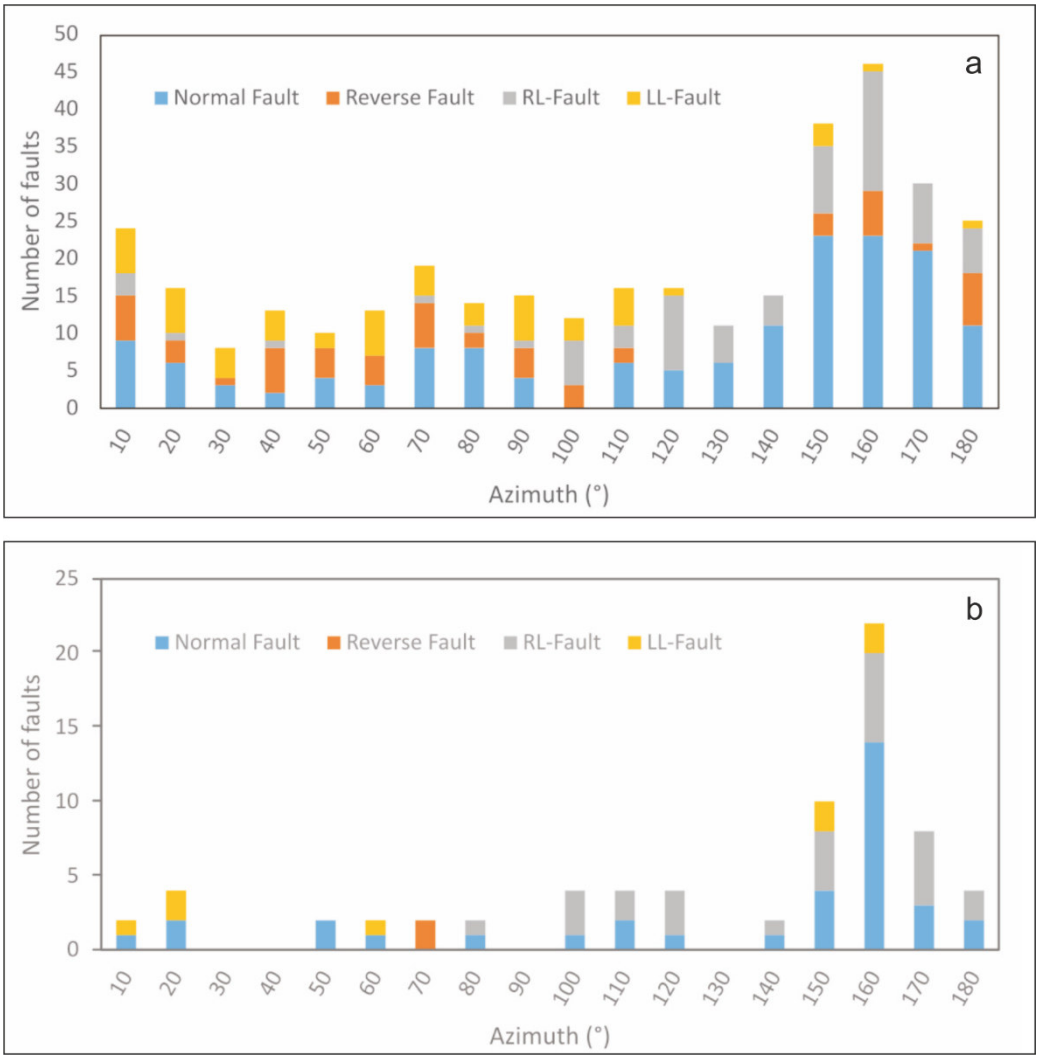

Figure 6. a) Azimuthal distribution of the entire dataset of shear planes distinguished by kinematic; b) Azimuthal distribution of the selected shear planes showing two generations of striae, distinguished by kinematic.

Figure 7

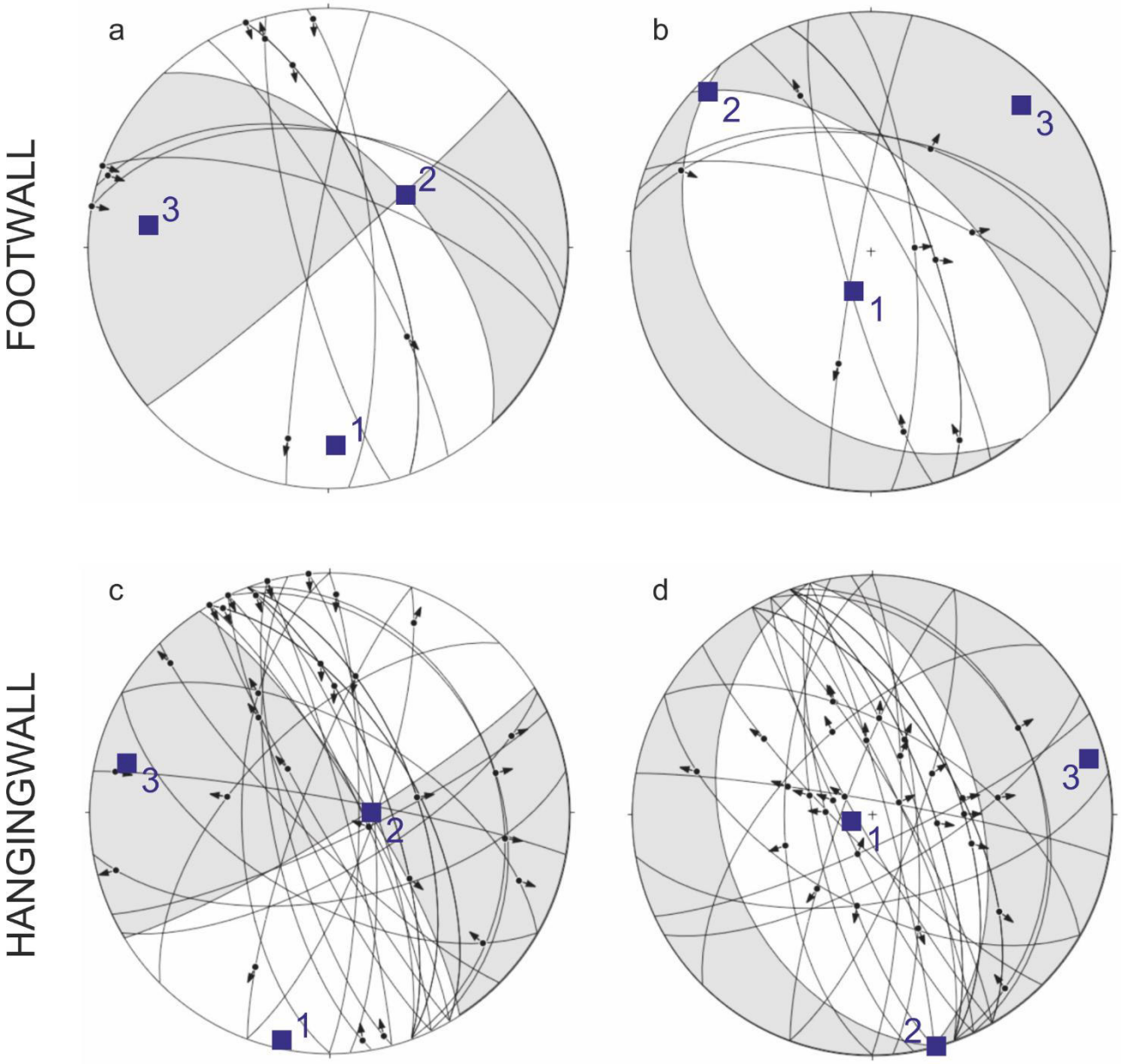

Figure 7. Moment tensor solutions resulting by fault inversion analysis of shear planes: a) plot results from older and (b) the youngest kinematics obtained from the data falling within the footwall; c) plot results from older and (d) the youngest kinematics from data falling within the hangingwall. Black dots indicate the rake values and black arrows the direction and the sense of movement. Blue squares represent the main axes of stress: 1= σ_3; 2= σ_2; 3= σ_1.

Figure 8

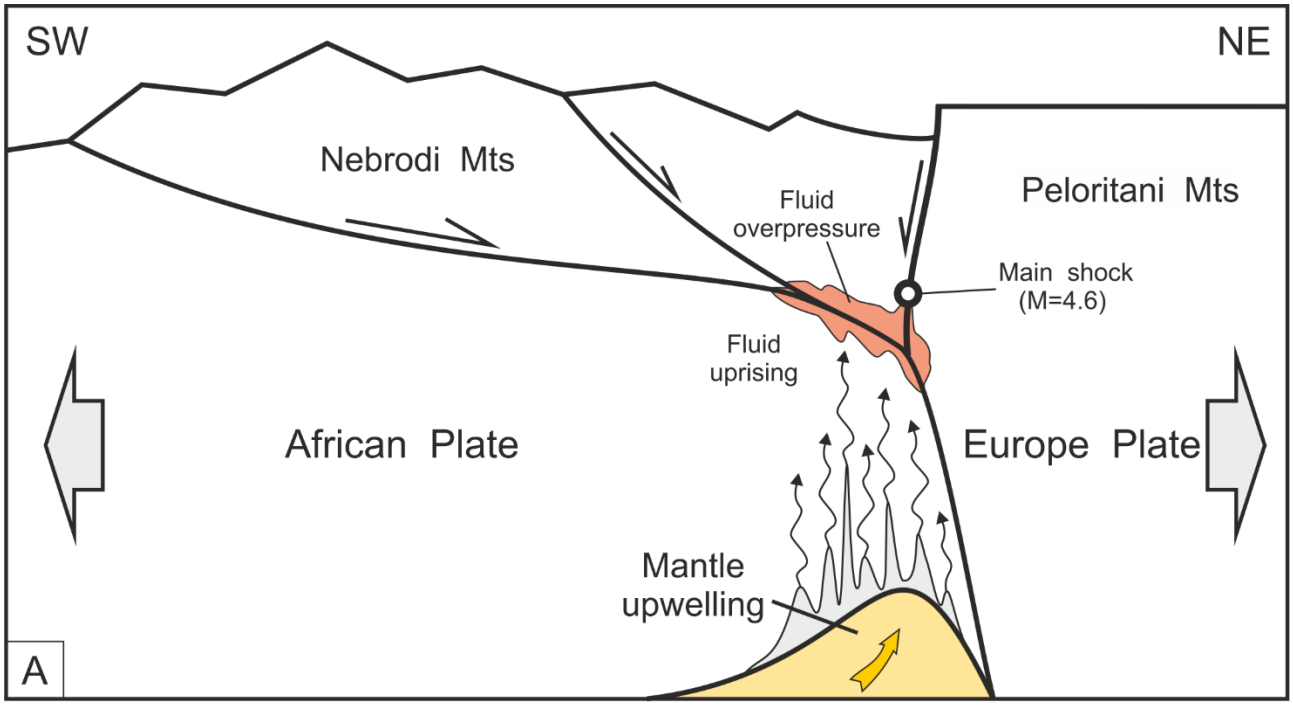

Figure 8. Schematic transect across the boundary between Nebrodi Mts. and Peloritani Mts., at the southern termination of the Calabrian, where diffuse normal faulting along previous thrust and high-angle strike-slip faults occurs. The Mantle upwelling, the fluid migration towards the surface and the fluid overpressure region at depth, invoked to model our results, are drawn.